On the potential for automated realtime detection of nonlinear internal waves from seafloor pressure measurements

Uwe Stöber [*1,2] and James N. Moum[2]

[1]Institut für Umweltphysik, Universität Bremen, Otto-Hahn-Allee, 28359 Bremen, Germany
[2]College of Oceanic & Atmospheric Sciences, Oregon State University, Corvallis, OR, 97331-5503, USA

Abstract

Because of the large forces they exert, large amplitude, highly nonlinear internal waves (NLIWs) represent a potential danger for offshore structures. This threat has prompted expensive operational observations to guarantee the safety of drilling platforms. The potential for automated detection using seafloor pressure measurements is investigated here, using data from New Jersey's continental shelf. The detection algorithm is first tested using the complete time series. Detection in the pressure record is verified by comparison to coincident velocity measurements permitting identification of false positives and false negatives. The detection algorithm achieves 100% success for NLIWs with pressure amplitude $> 250\,\mathrm{Pa}$, roughly equivalent to vertical velocity $0.1\,\mathrm{m\,s^{-1}}$, or a moderately energetic NLIW on New Jersey's continental shelf. Executed in pseudo-realtime mode, to simulate an automated detection scheme, waves $> 250\,\mathrm{Pa}$ are accurately detected with 1 h delay.

Keywords: nonlinear internal waves, detection algorithm, realtime detection, offshore platform safety, inexpensive measurements

*ustoeber@uni-bremen.de

1 Introduction

Large amplitude nonlinear internal waves (NLIW) have been observed all over the world [1]. They are found as depression waves, where they depress a near-surface pycnocline and as elevation waves, where they elevate a near-bottom pycnocline [2]. Due to their large velocities, NLIWs represent a potential danger to offshore drill rigs. The maximum force caused by a NLIW associated with a peak horizontal velocity of $2.1\,\mathrm{m\,s^{-1}}$ compares with the force exerted by a surface wave with wavelength 300 m and wave-height 18 m [3]. Using limited observational data of a NLIW in the northern South China Sea, Cai et al. [4] conclude that NLIWs can exert much larger forces and torques on a structure than surface waves. In the southern Andaman Sea, NLIWs may cause drill-ship offsets of more than 20 m and significant increases in anchor tensions [5]. In one case, anchor tension increased by a factor of 2.

Motivated by the threat to offshore structures, Hyder et al. [6] deployed a mooring in the northern Andaman Sea to observe NLIWs. From these observations, they developed a local prediction table based on tidal range. However, while it may be possible to predict internal tides (and from these, NLIWs) in enclosed basins from local surface tides and stratification at generation sites, it has been argued [7, 8] that remotely-generated internal tides with unpredictable phases can modulate internal tide and NLIW generation on continental shelves exposed to large ocean basins. Consequently, direct observations are necessary to provide alerts of NLIW activity.

NLIWs propagating at shallow water depths can be detected by synthetic aperture radar (SAR) imagery due to their characteristic patterns in sea surface roughness [9]. Satellite imagery provides snapshots of the 2D surface structure of NLIWs, but long time intervals between successive images at fixed locations preclude tracking [10]. Local SAR stations [11] along the coast may provide means for permanent operational wave detection, but are confined to near-shore observations.

In November 2008, Fugro GEOS Ltd deployed a Soliton Early Warning System (SEWS) in the Andaman Sea to support a 3-month drilling campaign [10]. SEWS consisted of two moorings, each equipped with an Aanderaa Doppler Current Sensor 3900 in the hull of the surface float, a Teledyne RDI 75 kHz Long Ranger Acoustic Doppler Current Profiler suspended 10 m below the buoy, and three Seabird SBE-37 temperature and conductivity sensors at 50 m, 80 m, and 110 m below the sea surface. The sampling interval was 2 min and data was transmitted onshore via the Iridium satellite network every 10 min, where an oceanographer on duty interpreted the data and informed the drill rig crew about incoming NLIWs. Several warning levels were based on predetermined thresholds of the NLIW's horizontal particle velocity (Table 1). The danger from internal solitons was considered so critical that the drilling activity would have had to be halted if SEWS was not operational.

Realtime comprehensive observation where all data are transmitted onshore and interpreted by on-duty personal is cost-intensive in both instrumentation and personnel. In addition, surface buoys for the satellite link are exposed to extreme weather conditions and potential collision with ships. Even subsurface buoys with reduced instrumentation such as less expensive single-beam ADCPs require considerable effort during deployment and are exposed to potential damage from fishing activities.

On the continental shelf, pressure measurements at the sea floor permit direct detection of NLIWs [12, 13]. For this purpose, simple instrumentation that is easily deployed on the seafloor for periods up to many months has been developed by our group (Fig. 1). Consequently, it seems possible to detect the internal waves in-situ and transmit an alert that contains only few variables such as the time of its detection, whether it is a depression or elevation wave, and its amplitude. The in-situ processing reduces the amount of data to a degree that the alert may be transmitted acoustically. By combining alerts from multiple seafloor sensors, the speed and direction of the wave can be determined by onshore processing.

In-situ detection of a pressure signal and acoustic transmission to surface buoys is used by Tsunami Early Warning Systems (TEWS) like NOAA's DART (Deep-ocean Assessment and Reporting of Tsunamis) program [14]. For the most part, deep-ocean seafloor pressure signals are uncomplicated by the presence of NLIWs [15] which are common on continental shelves [16] and tsunami detection is thus somewhat simplified there. On the other hand, tsunamis will be part of the continental shelf signal. While detection of tsunamis on the shelf will be of little help

Table 1: Warning levels and actions to be taken by the drill rig crew during the Soliton Early Warning System (SEWS) operation [from 10].

soliton velocity amplitude (kts)	($m\,s^{-1}$)	warning level	action on rig
< 1.5	< 0.8	low	none
$1.5 - 2.0$	$0.8 - 1.0$	medium	probably none
$2.0 - 3.0$	$1.0 - 1.5$	high	tighten anchor wires and standby
> 3.0	> 1.5	very high	prepare for possible disconnect

Figure 1: Deployment of a seafloor pressure instrument from a research vessel in Puget Sound. This version contains a Paroscientific model 6000-200A pressure transducer which has been optimized for maximum resolution. Visible at the top is a power plug. Inside the top end cap is an acoustic transducer. A unique coded sequence sent to this transducer triggers a logic sequence that burns a wire, releasing the weight at bottom and allowing the instrument to surface with the bottom end pointed upward. A GPS antenna in the end cap receives position and time, which are broadcast as a 900 Mhz digital radio signal through a separate antenna. The radio signal and flasher aid in shipboard recovery.

to an early warning system, the difference in spatial scales permit easy separation from NLIWs in a properly-designed seafloor array.

Here, we demonstrate a simple algorithm to detect NLIWs in observed pressure signals. This is accomplished by postprocessing of existing data with the intention that it could be applied to realtime in-situ measurements. We have not yet built this algorithm or transmission capabilities into our instruments. The calculation reported here is intended as a feasibility test of the procedure.

The data used in this study were recorded during the Shallow Water '06 Experiment (SW06) off the coast of New Jersey [17], from which depression waves were clearly identified from two seafloor pressure sensors [13]; however, no objective method to identify the wavetrains was applied. The record from the first sensor is 50 days long from July 29 to September 17, 2006 at mooring SW37 (72 m depth; 39°4.1′ N 73°10.1′ W, see Fig. 2). The record from a second seafloor pressure sensor is 47 days long at mooring SW38 (79 m depth; 39°1.2′ N 73°3.4′ W), from July 29 to September 14, 2006. The sampling rate was 1 Hz for both data sets.

For reference, a separate detection algorithm is applied to vertical velocity data recorded by a 500 kHz Sontek Acoustic Doppler Profiler (ADP) on SW37 and a 300 kHz RDI Acoustic Doppler Current Profiler (ADCP) on SW38, both sampled at 1 Hz and averaged over 30 s. Details of the measurements are given by Moum and Nash [13] who examined spectrograms of bottom pressure to identify NLIW signatures in the $1-10$ mHz range and verified these signals by comparison to predicted pressure estimated from measured velocity. They selected NLIWs subjectively based on visual inspection. Using shipboard and moored data, Shroyer et al. [18] studied

the properties of the NLIWs from their formation at the shelf break to the propagation over the shelf, but did not further analyze the seafloor pressure data.

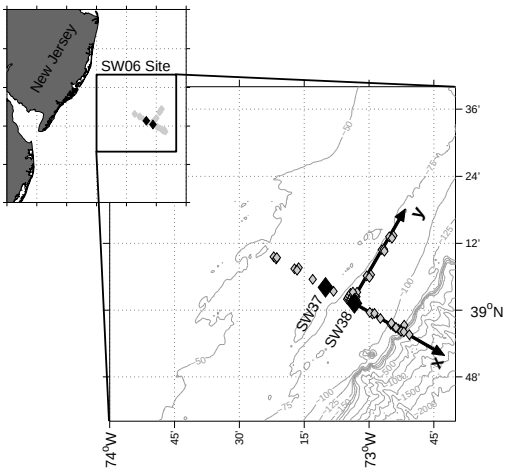

Figure 2: Location of the Shallow Water '06 site with moorings SW37 and SW38 represented as black diamonds. Other moorings are plotted in gray. Axes indicate the co-ordinate system used by Shroyer et al. [18].

Here, we apply a detection algorithm to seafloor pressure measurements that could lead to realtime automated detection of NLIWs without on-duty personnel or expensive instrumentation. We proceed as follows: We first identify the frequency bands of the NLIWs in the spectrogram of bottom pressure (section 2), and describe the detection algorithm as it is applied to the full data record (section 3); results are presented in section 4. We then apply the algorithm in pseudo-realtime mode and show that it can be efficiently implemented with 1 h delay (section 5). There follows a discussion of the influence of noise and the relationship of seafloor pressure to near-surface horizontal particle velocity as an indicator of potential harm to offshore platforms (section 6). We end with a summary and conclusions (section 7).

2 Identification of Frequency Bands

Processes over a wide range of frequencies contribute to the variability of the seafloor pressure signal over New Jersey's continental shelf. The strongest components are the tides (Fig. 3a), wind waves at $>$ 100 mHz and swell at $10 - 50$ mHz (Fig. 3b). The strongest NLIWs, appearing between August 18 and August 22, have a clear signature that is centered around 2.2 mHz.

It may be tempting to choose a narrow frequency band for detection to suppress as much of the other frequency content as possible, but since a NLIW is a narrow, one-sided signal in pressure [12], it is composed of a range of frequencies. Experiments using varying filter frequencies indicate that most of the relevant signal is retained using the bandpass filter indicated in Fig. 3d with high-pass cutoff at 0.17 mHz and low-pass cutoff at 7.8 mHz.

3 Detection algorithm

Our NLIW detection scheme (Fig. 4) compares the filtered pressure amplitude, p_f, and the amplitude of its time derivative, $(\mathrm{d}p/\mathrm{d}t)_\mathrm{f}$, to a threshold value selected from statistics of the overall signals. Subsequent criteria are set to refine the decision making. The objective is to detect a group of NLIWs and to then assess certain properties of the largest wave in the group: namely, the wave amplitude (in pressure) and its sign (depression or elevation). Detection is verified or determined to yield either a false positive or false negative result by comparison to coincident records of vertical velocity, w - in particular the filtered vertical velocity (w_f) at mid-water column. Unfortunately, pressure does not uniquely determine velocity (which is the critical factor in offshore structure integrity); we show in sec. 6 how these are related. Use of the time derivative of the pressure signal ensures that a pressure peak also has the characteristic steepness of a NLIW.

The detection threshold for waves is determined from the histogram of $|p_\mathrm{f}|$ (Fig. 5). A linear fit in the inflection point region intersects the pressure axis [19]. For a typical 5-day period the intersection occurs at 110 Pa (Fig. 5). This value is further multiplied by the threshold multiplier given in Fig. 4, e.g. 1.2 for pressure; this reduces false

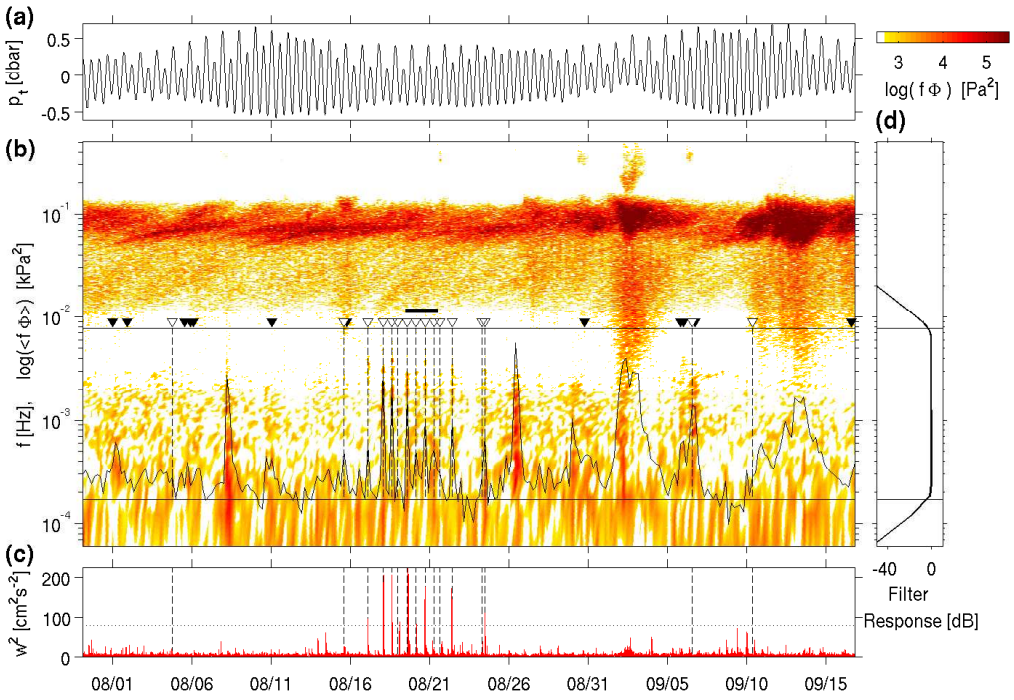

Figure 3: (a) Low-passed (9 h) seafloor pressure time series at SW 37. (b) Variance-preserving spectrogram of the high-passed (9 h) seafloor pressure. The line plot represents the average spectral energy in the frequency band 0.17 – 7.8 mHz. (c) Vertical velocity variance, w^2, at 31 m depth indicating the presence of NLIWs. The dotted line represents the $9\,\mathrm{cm\,s^{-1}}$ level. (d) Response of the Butterworth filter that is applied to the time series for automatic detection. Black horizontal lines in b) denote the limits of the Butterworth bandpass filter; black triangles indicate times of NLIWs as detected in pressure by the automated procedure, white triangles and dashed lines mark NLIWs that are also detected in w_f. A thick solid line above the triangles marks the time period shown in detail in Fig. 7.

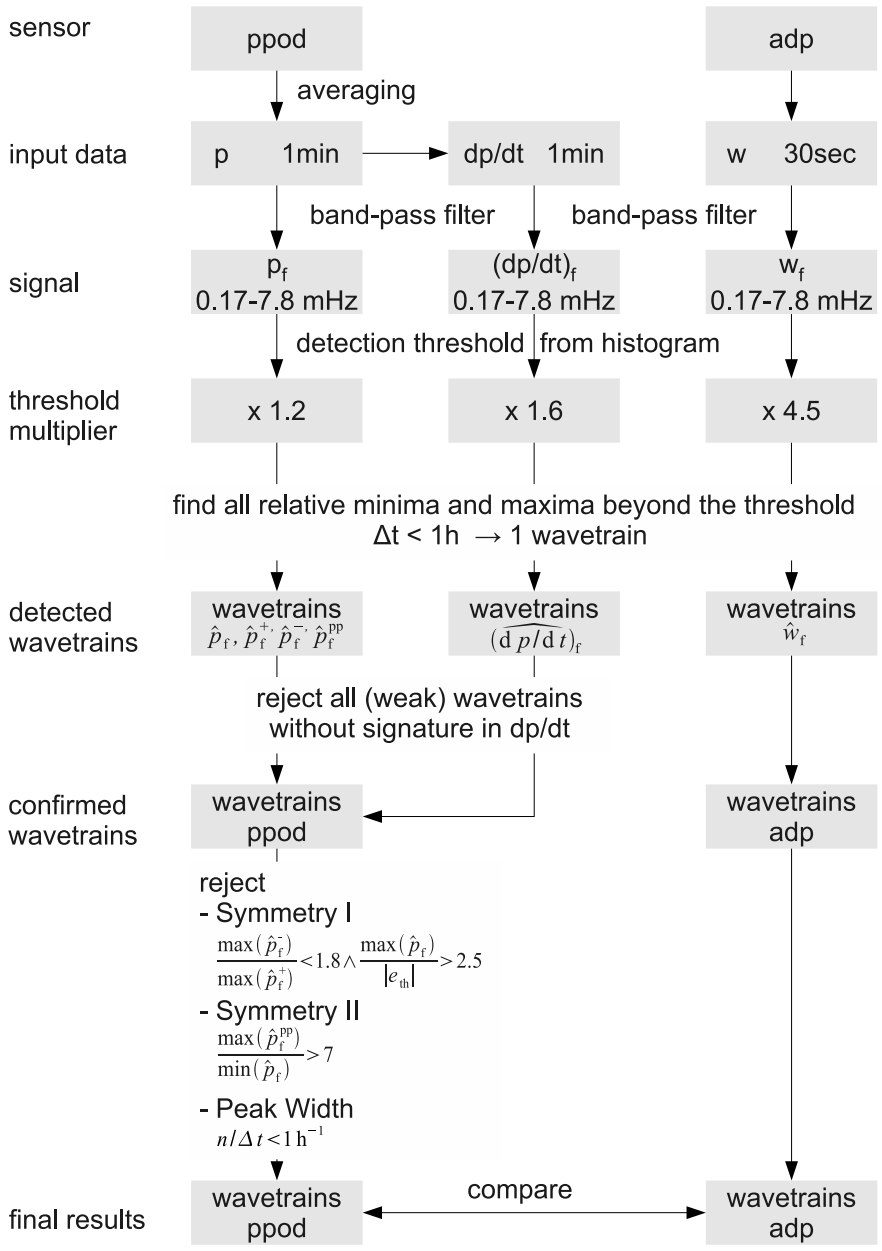

Figure 4: Flow chart of the detection mechanism with the rejection scheme for depression waves during detection in the complete data set. See text for description.

positive detections to a reasonable number. The multipliers were chosen subjectively based on the signal/noise ratio (S/N, Fig. 6) and the sensitivity of the application with regard to false positive and false negative detection. For high S/N, the wave signatures clearly stand out from noise and a large multiplier keeps the detection threshold high enough that it is not exceeded by noise. Low noise in high S/N yields also a narrower histogram where the linear fit in the inflection point intersects the abscissa at a low value, which may be compensated by a higher multiplier. A low multiplier yields in general a low detection threshold with more false detection, while a higher value misses weak waves. The detection threshold in our example for pressure is $e_{\mathrm{th}} = 110\,\mathrm{Pa} \times 1.2 = 132\,\mathrm{Pa}$ (Fig. 4). This procedure for determining the multiplier was repeated for $(\mathrm{d}p/\mathrm{d}t)_{\mathrm{f}}$ and w_{f}.

Using histograms to determine the detection threshold requires a certain minimum amount of data to ensure a regular and smooth shape of the histogram. In this study a minimum of 4-5 days of measurements were necessary. While this is a long time for a system that should work on a realtime basis, once the histogram is established and the detection threshold is determined, it may be retained for the duration of the deployment or updated using past, stored data on a regular basis.

In the next step all relative minima and maxima beyond the detection threshold are determined. If the time difference between two consecutive peaks is less than 1 h, we assume they belong to the same wave group and make a single detection for the wave group. Depending on the sign of p_{f}, the wavetrain's type is assigned depression or elevation. Every detected wavetrain is assigned a number for identification (cf. example in Fig. 7); wave amplitudes ($\hat{p}_{\mathrm{f}}$) peak-to-peak amplitudes ($\hat{p}_{\mathrm{f}}^{\mathrm{pp}}$), and wave sign are saved. $\hat{p}_{\mathrm{f}}^{\mathrm{pp}}$ is determined from consecutive peaks. Amplitudes of $(\mathrm{d}p/\mathrm{d}t)_{\mathrm{f}}$ and w_{f} are also saved for each wavetrain and indicated by $\hat{\cdot}$-signs.

There exist both false positives (detection of waves from the pressure series where none exists in the w_{f} series) and false negatives (non-detection of waves in the p_{f} series that are obvious in the w_{f} series, Table 2). Most false positives in p_{f} have no signature in $(\mathrm{d}p/\mathrm{d}t)_{\mathrm{f}}$ and are therefore rejected. Further tests require that the waves are one-sided (not symmetric) and have a reasonable peak width. Three tests

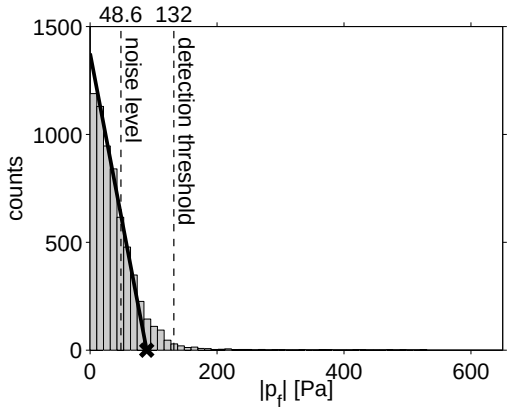

Figure 5: Histogram of the filtered pressure data recorded at SW37 from August 17, 20:00 UTC to August 22, 12:00 UTC. A 2-day section of the data is shown in Fig. 7. The black line is fitted to the slope of the histogram and intersects the ordinate axis at 110 Pa (black x).

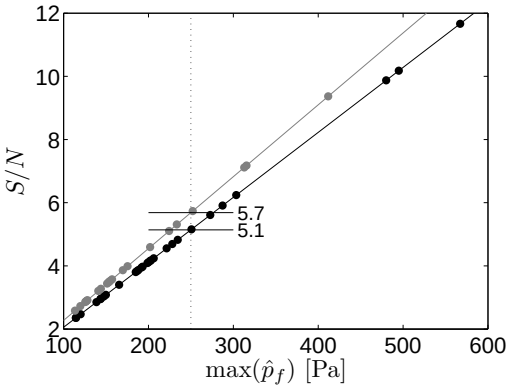

Figure 6: S/N as function of pressure amplitude at SW37 (black) and SW38 (gray). Signals are the maximum amplitudes of detected wavetrains, noise is the standard deviation in the absence of wave signatures. The values of S/N at the thresholds for 100% detection are marked.

Table 2: Errors that occur in the detection process and their signature in the pressure p and vertical velocity w signals.

error name		detection	
		p	w
Type I	false positive	yes	no
Type II	false negative	no	yes

are applied as follows (in each case, the constants were empirically-defined):

1. *Symmetry I*: Waves with near-equal amplitude maxima and minima are rejected if

$$\frac{\max\left(\hat{p}_\mathrm{f}^+\right)}{\max\left(\hat{p}_\mathrm{f}^-\right)} < 1.8 \quad \text{for elevation waves or} \quad (1)$$

$$\frac{\max\left(\hat{p}_\mathrm{f}^-\right)}{\max\left(\hat{p}_\mathrm{f}^+\right)} < 1.8 \quad \text{for depression waves,} \quad (2)$$

where $\hat{p}_\mathrm{f}^+$ and $\hat{p}_\mathrm{f}^-$ represent the absolute values of all positive and negative amplitudes of a detected wavetrain. Since conditions (1) and (2) reject small amplitude wavetrains that exceed the threshold e_th on both sides because of noise, it is also required that

$$\frac{\max\left(\hat{p}_\mathrm{f}\right)}{|e_\mathrm{th}|} > \begin{cases} 2.5 & \text{(all data)} \\ 1.9 & \text{(realtime)} \end{cases} \quad (3)$$

$\hat{p}_\mathrm{f}$ includes the absolute value of all positive and negative amplitudes of the wavetrain. The requirement for pseudo-realtime processing is stricter because the dynamic threshold e_th depends on S/N that changes in the course of the time series. If Eq. (3) *and* either Eq. (1) or (2) are satisfied, the signature is not considered a NLIW and rejected.

2. *Symmetry II*: Wavetrains with both large positive and negative amplitudes that were not already rejected due to symmetry I, are rejected if the peak-to-peak amplitude $\hat{p}_\mathrm{f}^\mathrm{pp}$ is much larger than the smallest detected amplitude of the wavetrain:

$$\frac{\max\left(\hat{p}_\mathrm{f}^\mathrm{pp}\right)}{\min\left(\hat{p}_\mathrm{f}\right)} > 7. \quad (4)$$

Three false positives were rejected by this test. Two of them are near-sinusoids of a single cycle in p_f with a period of 45 minutes and show no signal in the velocity observations. One of the two events is due to the change in hydrostatic pressure associated with a front that passed over the lander indicated by a temperature drop of 0.5 °C at the seafloor. The third false positive consists of positive and negative peaks of 10 min width and lasts in total about 12 h. It has no signatures in velocity and temperature and no associated events in the observed wind field. Clearly, none of these signals was associated with a NLIW. While it is possible that this condition eliminates the signature of waves in the process of polarity reversal, this typically occurs in quite shallow water (where the pycnocline depth is roughly 1/2 the water depth) and significant wave energy has already been lost to dissipative processes. Our experience is that these waves have weakened considerably [20] and are of minimal interest for our purpose.

3. *Peak Width*: All wavetrains that consist of one wide peak are rejected. We impose a minimum number n of peaks per time span Δt and reject all hits with

$$\frac{n}{\Delta t} < 1\,\mathrm{h}^{-1}. \quad (5)$$

4 Results

Our algorithm detects 4 NLIW signatures in the 2-day pressure time series shown in Fig. 7a,b. One of these detected NLIW groups does not exist in the w_f signal (Fig. 7c) and the algorithm misses a wave group that is clearly detected in w_f. This series provides an instructive example to indicate how the algorithm works and where it fails. Wave group #2

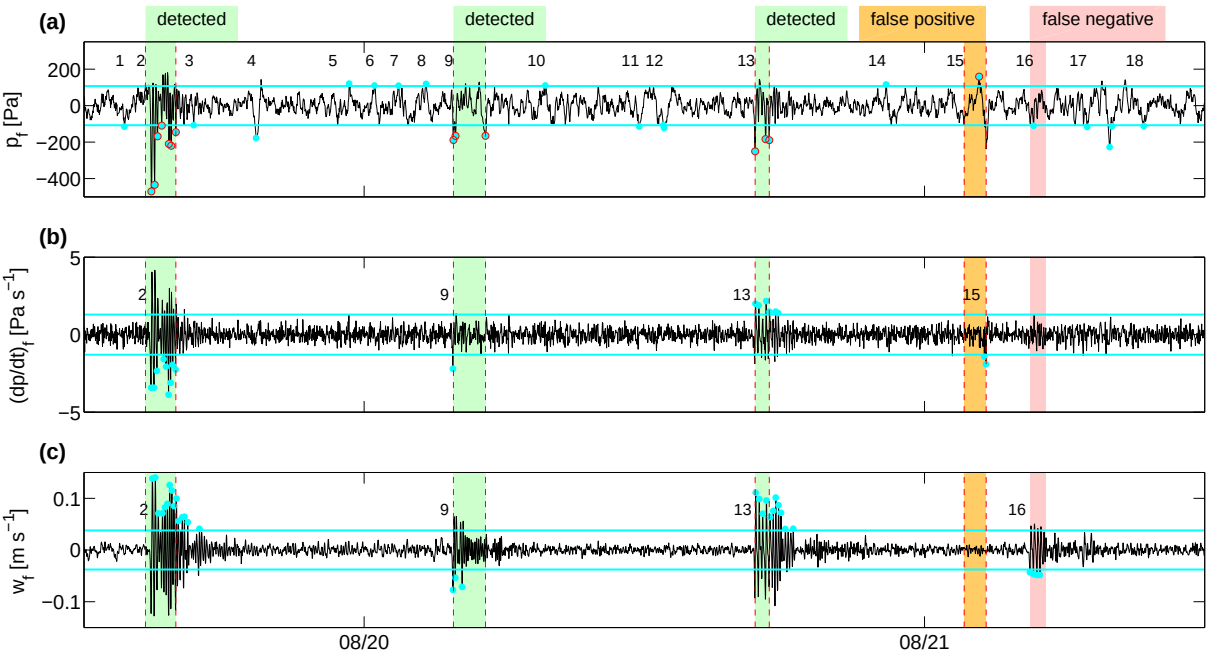

Figure 7: 2-day section of the detection results for SW37. Horizontal blue lines indicate the detection threshold for each signal. Blue dots mark peaks that exceed the threshold on the side of larger average amplitude. Red circles in a) mark confirmed waves and vertical red dashed lines mark confirmed wave groups remaining after the rejection scheme has been applied. Successful detection is indicated by green shading, false positives by orange, and false negatives by red. Wave groups that exceed the pressure detection threshold are assigned a number that is shown in a) and echoed in b), c).

shows seven pressure spikes that fall below the lower detection threshold as well as several that lie above the upper detection limit. Since the time separation between these spikes is < 1 h, they are assigned to the same group. Because the largest amplitude indicates a negative pressure fluctuation (hence a depression wave), the wave group is determined to be one of depression. This largest amplitude ($\max \hat{p}_\mathrm{f}$) is determined to be the most significant event to report and selected for the analysis of detection statistics to follow. Since it is confirmed by the coincident w measurement, it is shaded green and determined to be a successful detection. Waves # 9 and 13 have considerably different character and amplitude, but the same procedure is followed to determine these to be successfully detected. The false positive (wave #15) indicated in Fig. 7 is clearly defined as such by the absence of any significant signal in w_f. Wave #16 has small amplitude though it is clearly defined by w_f; the pressure amplitude marginally falls below the lower threshold level. However, the wave is rejected on the basis of small $(\mathrm{d}p/\mathrm{d}t)_\mathrm{f}$, yielding a false negative result.

To summarize the result shown in Fig. 7, three of four (75%) of the detected wavetrains in the pressure time series are identified in the vertical velocity signal, resulting in one false positive or a Type I error of 25%. Three of four (75%) of the wavetrains in vertical velocity are detected in the pressure signal. Thus, there is one false negative or a Type II error of 25%.

The detection algorithm was applied to the complete time series recorded with mooring SW37 (July 30, 15:00 UTC to September 17, 9:00 UTC), excluding data recorded during Tropical Storm Ernesto (September 1, 12:00 UTC to September 4, 13:00 UTC) and during Tropical Storm Florence (September 10, 12:00 UTC to September 15, 12:00 UTC). During the storms, the signal of the surface waves superposes the NLIWs (Fig. 3b) and makes automated detection impossible. In the remaining time series, 29 wave groups are identified in the pressure signal and 66 are identified in the vertical velocity signal (Table 3). Moum and Nash [13] subjectively selected 79 NLIWs in the vertical velocity signal of the total time period including the Tropical Storms. Sixteen wave groups were detected in both p_f and w_f and are therefore considered properly detected. Thus, 55% of the NLIWs were correctly detected in p_f; this corresponds to a Type I error of 45%. But

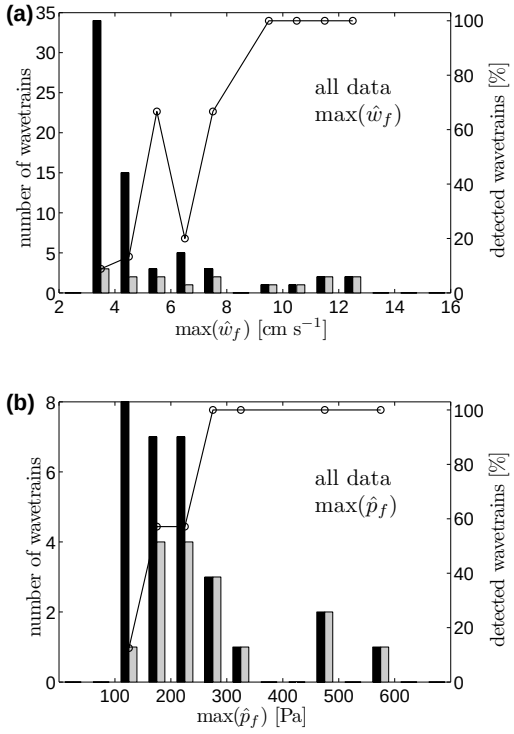

Figure 8: Number of wavetrains that are detected in a) w_f (black) and b) p_f (black) at SW37 and that are also detected in the respective other signal (gray), i.e. that are successfully identified. The black line shows the number of successfully detected wavetrains in percent.

only 24% of all signatures in w_f, our reference, were detected; the Type II error is 76%.

The detection probability depends strongly on the amplitudes $\hat{p}_\mathrm{f}$ and $\hat{w}_\mathrm{f}$ (Fig. 8). NLIWs with w_f amplitude greater than $9\,\mathrm{cm\,s^{-1}}$ were always detected (Fig. 8a). When NLIWs with $\max \hat{w}_\mathrm{f} < 9\,\mathrm{cm\,s^{-1}}$ were detected, less than 80% of their signatures were detected in $\hat{p}_\mathrm{f}$. In the same way the false detection probability depends on amplitude (Fig. 8b). There is no false detection for $\max \hat{p}_\mathrm{f}$ amplitudes larger than 250 Pa, but $< 60\%$ are correctly identified below this threshold.

The detection algorithm was applied to the moored data at SW38 as well with similar results. Perfect detection was achieved for $\max(\hat{p}_\mathrm{f})$ amplitudes

[1] Only if wavelets are used to filter w, otherwise no threshold for w.

Table 3: Detection results for retrospective detection on the complete data set and realtime detection with 1 h delay. The numbers n of detected wave trains in pressure p_f, vertical velocity w_f, and both time series are complemented by the thresholds p_th and w_th for 100% detection.

	p_th	$n(p_\mathrm{f})$	n(both)	$n(w_\mathrm{f})$	w_th
all data					
SW37	250 Pa	29	16	66	$9\,\mathrm{cm\,s^{-1}}$
SW38	250 Pa	22	12	62	$13\,\mathrm{cm\,s^{-1}}$
realtime					
SW37	250 Pa	49	17	55	$9\,\mathrm{cm\,s^{-1}}$
SW38	200 Pa	42	15	55	$[23\,\mathrm{cm\,s^{-1}}]^1$

$>$ 250 Pa. However, because NLIW amplitudes were generally smaller at SW38, Type II errors were larger (81%).

5 Realtime Detection

For an effective warning system, NLIWs must be detected in near-realtime with a minimum delay between the wave's passage past the observation point and our algorithmic detection of the wave from the sampled data. The ability of our algorithm to detect NLIWs from realtime was tested by applying the detection algorithm to a sliding 5 day window sampled from the complete data set at SW37. This was constructed from the start of the data set, the algorithm applied and then the data set was advanced 1 h in time. To simulate a 1 h delay, only wavetrains with a signature in the last 1 h are taken into account for the detection statistics. The 1 h advance is nearly equivalent to 1/2 the time scale of the -3db high-pass cutoff point of the filter shown in Fig. 3c; the filter length precludes advancing the data in shorter increments.

For the SW37 time series, realtime detection yields similar results as retrospective detection on the full data set (Table 3, Fig. 9). A total of 49 wavetrains were detected in the pressure time series, compared to only 29 for retrospective detection. Since only one more wavetrain (17 compared to 16 before) is detected in both pressure and velocity, the number of false positives has almost doubled. Signatures in vertical velocity decreased from 66 (all data) to 55 (realtime), decreasing the number of false negatives. The decrease is, however, partly due to the first 5 days that serve only to determine the detection threshold and are not analyzed for NLIWs. The threshold for 100% remains at 250 Pa for pressure and $9\,\mathrm{cm\,s^{-1}}$ for vertical velocity.

At SW38, the number of waves detected in pressure doubled from 22 (all data) to 42 (realtime), while it decreased from 62 to 55 for the detection in vertical velocity. Fifteen waves were detected in both data sets, leaving again a higher rate of false positive detection and a lower rate of false negative detection than for detection in the complete data set. The threshold for 100% detection decreases for pressure (200 Pa instead of 250 Pa), but no such threshold exists for vertical velocity.

The maximum amplitudes of the waves detected in pseudo-realtime mode are slightly different compared to the detection using all data, so that the histograms (Fig. 8 and 9) are not identical. This is solely because the highpass filter is applied to different data segments in each case, thereby resulting in different low-frequency variations and slight changes in amplitude. The scatter is however small (Fig. 10) and shows no systematic over- or underestimate for one method. Correlation coefficients are $r > 0.98$ and $r > 0.97$ for $\max(\hat{w}_\mathrm{f})$ and $\max(\hat{p}_\mathrm{f})$, respectively.

We tested an alternative method of isolating the NLIW signal using wavelet decomposition of the pressure record. This method yields results marginally different from simple Fourier filtering and slightly different amplitudes of the detected waves permit to define a threshold for perfect detection at SW38 that is $23\,\mathrm{cm\,s^{-1}}$. However, wavelet decomposition incurs significantly greater computational expense, and it is not clear that the marginal improvement in detection is justified.

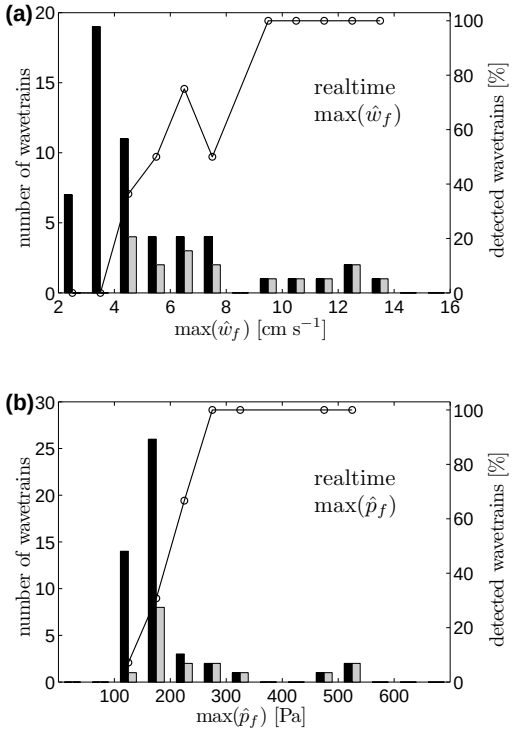

Figure 9: Number of wavetrains the realtime algorithm detected in a) w_f (black) and b) p_f (black) at SW37 and that are also detected in the respective other signal (gray), i.e. that are successfully identified. The black line shows the number of successfully detected wavetrains in percent.

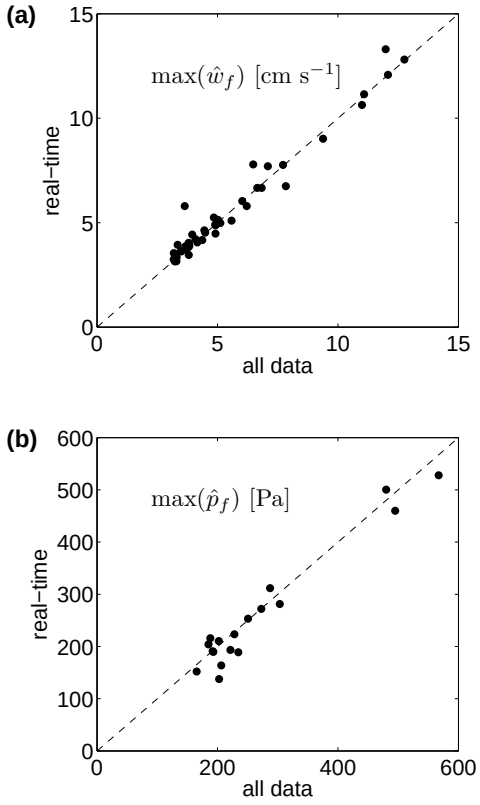

Figure 10: Scatter plots of detected maximum amplitudes in pseudo-realtime mode and using all data for velocity (max($\hat{w}_\mathrm{f}$), a) and pressure (max($\hat{p}_\mathrm{f}$), b) at SW37.

6 Discussion

A direct comparison of the errors in detection when all data is used (Fig. 11) reveals that Type I errors at SW37 and SW38 show the same characteristics: False positive detection falls from 100% to 0% between 125 and 275 Pa. Type II errors decrease rapidly at both sites, but at different velocity thresholds. At SW37 false negative detection is 0% at 9 cm s^{-1}, at SW38 it is 13 cm s^{-1}. In order to determine the reasons for this difference, we consider the noise in both data sets that is interpreted as the standard deviation in the absence of NLIWs from July 30, 20:00 to August 4, 12:00 (Table 4). Noise levels for vertical velocity at SW38 are 70% larger than at SW37. Consequently, S/N at SW38 is lower for any velocity amplitude. S/N for 9 cm s^{-1} at SW37 is 12.5, while it is 10.5 for the 13 cm s^{-1} at SW38. Noise levels for pressure are similar at SW37 and SW38 (Table 4), and so are the S/N of 5.1 (SW37) and 5.7 (SW38) required for 100% detection (Fig. 6).

For pseudo-realtime detection, Type I errors (false positive) vanish above 250 Pa (SW37) and 200 Pa (SW38). The Type II error (false negative) vanishes only at SW37, at 9 cm s^{-1}. At SW38, the false detection increases again to 50% after it reached 0% at 15 cm s^{-1} (Fig. 12). However, this is based on no more than 4 samples, i.e. 2 wavetrains that have no signature in pressure. The small number of stronger waves (7 for $\hat{w}_\mathrm{f} > 12.5$ cm s^{-1} limits statistical treatment. On the other hand, the fact that 100% detection beyond given thresholds is achieved suggests the potential for application in offshore platform

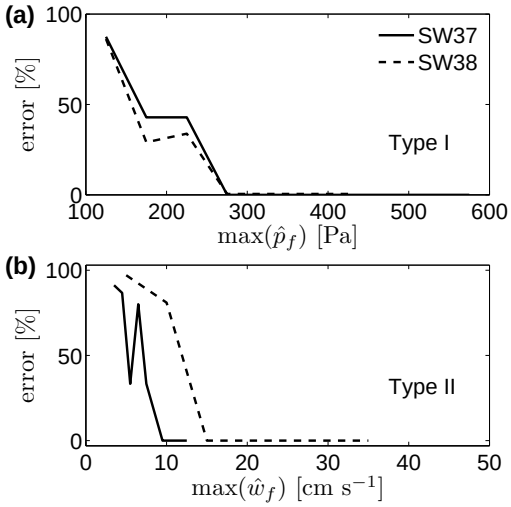

Figure 11: False positive (Type I error, a) and false negative (Type II error, b) detection at mooring sites SW37 (solid) and SW38 (dashed) for detection using the complete data set.

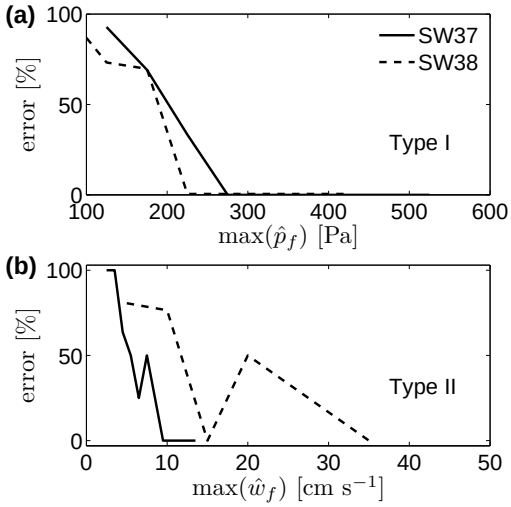

Figure 12: False positive (Type I error, a) and false negative (Type II error, b) detection at mooring sites SW37 (solid) and SW38 (dashed) for pseudo-realtime detection.

Table 4: Noise levels in pressure and vertical velocity at locations SW37, SW38 as represented by the standard deviation evaluated in the absence of NLIWs from July 30, 20:00 to August 4, 12:00.

	SW37	SW38
$N(p_\mathrm{f})$ [Pa]	48.6	44.0
$N(w_\mathrm{f})$ [cm s^{-1}]	0.72	1.24

safety.

It is horizontal velocity rather than pressure that directly relates to drag on a structure. Pressure is related to velocity through either a vertical integral of the vertical momentum equation or a horizontal integral of the horizontal momentum equation [12]. We follow each approach to get an assessment of the near-surface velocity signature associated with the seafloor pressure measurements, under conditions applicable to the New Jersey shelf in summer 2006. The first approach is based on a prediction derived from the Korteweg-de Vries (KdV) model [e.g. 21] for finite amplitude waves in a continuously-stratified environment.

We evaluate the KdV wave field using a range of 10 nearby observed density profiles (and no horizontal background flow). For each stratification, we vary the wave amplitude to obtain a range of seafloor pressure amplitudes. The predicted velocity field then provides us with the amplitude of near-surface horizontal velocity. These are represented by the gray-shaded envelope in Fig. 13a. In addition to assessing sensitivity to the range of observed stratification, we test sensitivity to mixed layer density and water depth. For fixed seafloor pressure amplitudes, KdV predicts increasing near-surface horizontal velocity for decreasing density difference between mixed layer and deep water, and for increasing water depth.

Pressure and velocity are also related through the horizontal momentum equation. With constraints, this permits an evaluation of the near-surface velocity dependence on seafloor pressure. For the second approach we consider a two-dimensional wave with phase speed c in x-direction. Neglecting viscous effects pressure p is related to horizontal velocity u by

$$p = -\rho_0 \int_{-\infty}^{x} \frac{\mathrm{D}u}{\mathrm{D}t} \mathrm{d}x' \qquad (6)$$

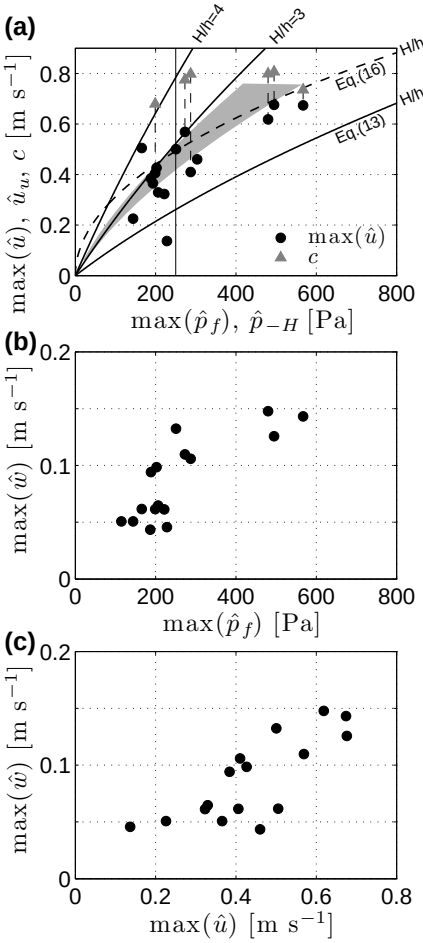

Figure 13: Wave properties. a) horizontal particle velocity amplitude in the upper layer versus seafloor pressure amplitude at SW37 (black dots). For wavetrains that were detected at both SW37 and SW38, phase velocities c were derived from the difference in the detection times and the distance between SW37 and SW38 (gray triangles connected by dashed lines to the corresponding $\max(\hat{u})$). The prediction from Eq. 12 is drawn for $H/h = 2$, 3, 4 and the average wave speed [13, 18, solid line]; the prediction from Eq. 16 is indicated by the dashed line; KdV predictions based on 10 nearby observed density profiles are displayed in grey. The vertical line indicates the threshold for 100% detection. b) vertical velocity amplitude versus seafloor pressure amplitude. c) vertical velocity amplitude versus horizontal velocity amplitude.

where

$$\frac{\mathrm{D}}{\mathrm{D}t} = \frac{\partial}{\partial t} + u\frac{\partial}{\partial x} + w\frac{\partial}{\partial z} \tag{7}$$

and ρ_0 is the density of sea water. If the wave propagates without changing its form at velocity c, the partial time derivative can be expressed by

$$\frac{\partial}{\partial t} = -c\frac{\partial}{\partial x}. \tag{8}$$

w is large at leading and trailing edges of the wave, where u and its vertical derivative are small. w is small at maximum isopycnal displacement, where u and $\partial u/\partial z$ are large. Thus, in both cases $w\partial u/\partial z$ is small compared to other terms and neglected in Eq. (7). Eq. (6) then implies that at any depth

$$p \simeq -0.5\rho_0 u(u - 2c), \tag{9}$$

where u is the wave-induced velocity. Conservation of mass requires that

$$\int_{-H}^{0} u\mathrm{d}z = 0, \tag{10}$$

where H is the water depth (neglecting any distortion of the free surface). For a rough estimate, we further assume a 2-layer fluid and Eq. (10) is integrated to obtain

$$hu_{\mathrm{u}} = (h - H)u_{\mathrm{l}}, \tag{11}$$

where u_{u} and u_{l} are the horizontal wave velocities in an upper layer (between h and the surface) and lower layer (between h and the seafloor), respectively. h is the depth where horizontal wave velocity changes sign and vertical velocity is largest. The maximum vertical velocities occur in the pycnocline during the wave event. h is thus the depth of the pycnocline during the wave event. The steady state pycnocline has the depth $h - A$, where A is the wave's amplitude. We use this unusual notation to obtain a simpler expression in our final result. A summary of the depth related variables is shown in Fig. 14.

Combining Eq. 9 and Eq. 11 yields expressions for the maximum amplitudes:

$$\hat{p}_{-H} = \frac{\rho_0}{2}\frac{h}{h - H}\hat{u}_{\mathrm{u}}\left(\frac{h}{h - H}\hat{u}_{\mathrm{u}} + 2|c|\right) \tag{12}$$

and

$$\hat{u}_{\mathrm{u}} = \frac{h - H}{h}|c| + \frac{h - H}{h}\sqrt{\frac{h}{h - H}c^2 + \frac{2\hat{p}_{-H}}{\rho_0}}. \tag{13}$$

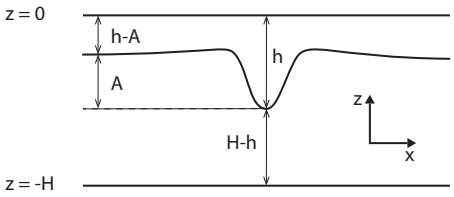

Figure 14: Definition of depth related variables. Note that h is not the pycnocline depth in steady state, but during the wave event when the pycnocline deflection is at its maximum.

As before $\hat{}$ designates amplitude, subscript u indicates the upper layer , and $-H$ indicates the seafloor. We thus obtained a relationship between seafloor pressure amplitudes ($\hat{p}_{-H}$) and near-surface horizontal velocity ($\hat{u}_\mathrm{u}$).

Alternatively Eq. (8) might be further simplified, because u and c have a similar absolute value [12, 22]. For depression waves, u and c have opposite signs near the seafloor, so that

$$\frac{\mathrm{D}}{\mathrm{D}t} \simeq 2u\frac{\partial}{\partial x} \tag{14}$$

and

$$p \simeq -\rho_0 u^2. \tag{15}$$

Then, the amplitude of pressure at the seafloor is approximated by

$$\hat{p}_{-H} \simeq \rho_0 \left(\frac{h}{h-H}\hat{u}_\mathrm{u}\right)^2. \tag{16}$$

Eq. (13) predicts the near-surface horizontal particle velocity of a NLIW based on the seafloor pressure amplitude, provided that the propagation speed and the depth of the pycnocline during the wave event are known. Both the KdV model and the momentum balance require thus a priori information about the stratification and NLIW properties.

A scatter plot of the measured amplitudes of the detected waves (Fig. 13a) confirms the general trend of higher velocities for larger pressure amplitudes. For completeness are shown comparisons of pressure and vertical velocity (Fig. 13b) as well as horizontal velocity and vertical velocity (Fig. 13c).

Apart from the general trend of higher velocities for larger pressure amplitudes, the ability to quantify $\hat{u}_\mathrm{u}$ for given $\hat{p}_{-H}$ is limited due to uncertainties in the prediction. For a wave of 250 Pa, the KdV model predicts a range of $0.4\,\mathrm{m\,s^{-1}} < \hat{u}_\mathrm{u} < 0.55\,\mathrm{m\,s^{-1}}$ while the horizontal momentum balance yields $0.25\,\mathrm{m\,s^{-1}} < \hat{u}_\mathrm{u} < 0.8\,\mathrm{m\,s^{-1}}$. For larger pressure amplitudes, the range of predicted $\hat{u}_\mathrm{u}$ becomes even larger, so that precise warning levels are difficult to define and will require adjustment at each site of operation.

7 Summary and Conclusions

The frequency band for automatic detection was chosen based on the NLIW signatures in the spectrogram. A 4-pole Butterworth filter was used to bandpass filter the pressure signal in the frequency band 0.17 mHz $< f <$ 7.8 mHz. A direct detection mechanism based on peak detection beyond a dynamic threshold was applied to the filtered pressure and pressure derivative. Peaks were grouped into wave trains and a rejection scheme was applied to sort out all detections that did meet a prescribed set of quantitative requirements (Fig. 4). For reference, results were compared to detection from vertical velocity signals.

Applied to the complete pressure data set of mooring SW37 (SW38), our detection algorithm detected 24% (19%) of the wave trains that were also detected in the reference measurements of the ADP (ADCP). Wave trains with vertical velocity $\geq 9\,\mathrm{cm\,s^{-1}}$ ($13\,\mathrm{cm\,s^{-1}}$) were always detected; the Type II error above that vertical velocity threshold is 0. A total of 55% (55%) of the detected wave trains in the pressure signal were also detected in the ADP (ADCP) reference record. For wave trains with amplitudes of more than 250 Pa detection was always correct; the Type I error above that pressure threshold is 0. The height of the threshold for 100% detection depends on S/N, which was between 5.1 and 5.7 for pressure and between 10 and 13 for vertical velocity in our measurements.

Pseudo-realtime detection with a maximum 1 h delay yields similar results as the retrospective detection applied to the full data set. Type I errors at SW37 (SW38) vanish above 250 Pa (200 Pa). Type II errors vanish at SW37 for $\hat{w} > 9\,\mathrm{cm\,s^{-1}}$. At SW38, wave signals were weaker, S/N was lower for both p and w, and a determination of Type II errors is difficult. For increasing delays, the detection results converge with the results using the entire data set. A further decrease in the delay results in Type I

and Type II errors that are no longer amplitude related. In order to compare the 1 h delay to the time scale of a NLIW, we define a wave period $T = 2L/c$, where L is the half width at half maximum of the peak. On the New Jersey continental shelf, T is typically between 5 and 15 min and 10 min for most waves. Thus, automatic detection requires at least 4 wave periods. At $0.8\,\mathrm{m\,s^{-1}}$, the waves propagate approximately 3 km from the point of detection. This provides some idea of the necessary separation between the detection site and that of the offshore structure of interest. The SEWS deployment in the Andaman Sea [10] specified a 10 h warning for large amplitude internal waves. At $0.8\,\mathrm{m\,s^{-1}}$ this is equivalent to a 29 km (plus 3 km for detection) required separation between detection site and structure.

On the New Jersey shelf, this detection algorithm reliably identifies NLIWs with $p > 250\,\mathrm{Pa}$. Adding a priori information and reducing automatic features might improve detection. The dynamic detection thresholds, for example, might be replaced by predefined static values. Then, the irregular occurrence of the NLIWs would no longer influence the threshold. Alternatively, the threshold can be increased to 250 Pa (after all, the waves discussed here belong to the weakest category in Table 1), where Type I errors vanish and non-detection of weak wave trains is accepted. A high threshold is favorable for single instruments. For a network of detectors, a comparison of the alerts can be used not only to determine wave speed and direction, but also to reject false positives at single detectors.

A major challenge remains to relate seafloor pressure amplitudes to near-surface horizontal particle velocities. There is a sizable range of possible horizontal velocities related to a given seafloor pressure amplitude. Depending on the approach, the prediction of $\hat{u}_\mathrm{u}$ requires either a representative density profile and evaluation based on KdV or other finite amplitude theory, or an estimate of the deflected pycnocline depth and wave speed (Eq. 13).

For detection at other locations some preliminary environmental information will be necessary. In particular, the stratification is critical to the relationship between $\hat{p}_{-H}$ and $\hat{u}_\mathrm{u}$ and may affect the choice of bandpass filter cutoff frequencies. Other environmental factors influence background pressure signals and hence, detection limits. Yang et al. [23] observed waves with seafloor pressure amplitudes of more than 4000 Pa in the South China Sea and conclude that the seafloor pressure signal of the NLIWs is large enough for detection. They show a 2500 Pa wave with horizontal velocities of about $1.5\,\mathrm{m\,s^{-1}}$. The seafloor pressure amplitudes correlate with their predictions from horizontal particle velocity.

Based on the above findings, the automatic detection algorithm requires a set of inputs that must be available prior to deployment:

1. S/N: For negligible Type I error, S/N should be 5.7 or better. If the noise level N is known from first test measurements, the signal strength that can be detected must be larger than $5.7 \times N$. S/N determines the thresholds for the detection mechanism either because a fixed threshold is chosen or because the multiplier has to be set for a dynamic threshold. A dynamic detection threshold requires 4 to 5 days of data. We used this scheme in our pseudo-realtime detection. Alternatively, it is possible to collect data for a certain amount of time, determine a detection threshold from this record and retain it for the rest of the deployment. While the former solution requires a lot of computation, the latter is insensitive to changes in S/N, just as a predefined parameter would be.

2. frequency band: Although the period of internal waves is typically of the order of minutes and thus the frequency band is roughly known, a precise choice of the frequency band limits improves S/N. If the frequency band is too narrow, the wave signatures do not reach full amplitude; If too broad, other signals dominate.

3. shape of the waves: The rejection process relies on symmetry, size and width of the peaks within a wave train. If no rough estimate of these magnitudes exists, the shape-based rejection scheme should not be applied.

4. stratification: The KdV model can be applied to relate pressure at the seafloor to near-surface particle velocities, if stratification is available. Observations of the wave's deformed pycnocline provide an alternative estimate of the horizontal particle velocity.

This study has considered only surface-trapped depression waves. While the algorithm in its current implementation is also able to detect bottom-trapped elevation waves ([2], for example), it can not find wavetrains with both polarities as observed, for instance, on the northwest shelf of Australia [24]. Nor can it detect symmetric NLIWs which exist if the sign of the cubic term in the extended Korteweg-de Vries equation is positive. Grimshaw et al. [25] provide global maps with coefficients that may serve as a guidance to determine the polarity of NLIWs.

Acknowledgements

This work was funded by the Office of Naval Research (N00014-08-1-0426) and the National Science Foundation (0751930). We thank Emily Shroyer for insightful discussions and providing guidance on how to use her NLIW analysis. Sam Kelly, Aurélie Moulin, Jonathan Nash and Matthias Zeeman provided helpful comments.

References

[1] Jackson CR. An Atlas of Internal Solitary-like Waves and their Properties. Global Ocean Associates; second ed.; 2004. `www.internalwaveatlas.com`.

[2] Moum JN, Klymak JM, Nash JD, Perlin A, Smyth WD. Energy transport by nonlinear internal waves. J Phys Oceanogr 2007;37:1968–1988.

[3] Du T, Sun L, Zhang Y, Bao X, Fang X. An estimation of internal soliton forces on a pile in the ocean. J Ocean Univ China 2007;6(2):101–106. Doi:10.1007/s11802-007-0101-y.

[4] Cai S, Long X, Gan Z. A method to estimate the forces exerted by internal solitons on cylindrical piles. Ocean Engineering 2003;30(5):673–689.

[5] Osborne AR, Burch TL, Scarlet RI. The influence of internal waves on deep-water drilling. J Petroleum Technology 1978;30(10):1497–1504.

[6] Hyder P, Jeans DRG, Cauquil E, Nerzic R. Observations and predictability of internal solitons in the northern Andaman Sea. Appl Ocean Res 2005;27(1):1–11.

[7] Kelly S, Nash J. Internal tide generation and destruction by shoaling internal tides. Geophys Res Lett 2010;.

[8] Nash JD, Kelly S, Shroyer EL, Moum J, Duda TF. On the futility of internal tide prediction on continental shelves. J Phys Oceanogr 2010;.

[9] Alpers W. Theory of radar imaging of internal waves. Nature 1985;314:245–247.

[10] Goff M, Jeans G, Harrington-Missin L, Baschenis C. Soliton early warning system for offshore applications. In: Oceanology International 2010. London ExCeL; 2010,March 9-11.

[11] Kropfli RA, Clifford SF. The Coastal Ocean Probing Experiment: Further studies of air-sea interactions with remote and in-situ sensors. In: Proc. IGARSS'96. Lincoln, Ne: Institute of Electrical and Electronics Engineers; 1996, p. 1739–1741.

[12] Moum JN, Smyth WD. The pressure disturbance of a nonlinear internal wave train. J Fluid Mech 2006;558:153–177. Doi:10.1017/S0022112006000036.

[13] Moum JN, Nash JD. Seafloor pressure measurements of nonlinear internal waves. J Phys Oceanogr 2008;38:481–491. Doi:10.1175/2007JPO3736.1.

[14] Lawson RA. Tsunami detection systems for international requirements. In: OCEANS 2007. 2007, p. 1 –7. doi:\bibinfo{doi}{10.1109/OCEANS.2007.4449208}.

[15] Baba T, Hirata K, Kaneda Y. Tsunami magnitudes determined from ocean-bottom pressure gauge data around Japan. Geophys Res Lett 2004;31. Doi:10.1029/2003GL019397.

[16] Aasen S, Mustapha Z, Schjolberg P, Elliott T. A deepwater tsunami surveillance system for Malaysia. In: OCEANS 2006 - Asia Pacific. 2006, p. 1 –7. doi:\bibinfo{doi}{10.1109/OCEANSAP.2006.4393971}.

[17] Tang D, Moum JN, Lynch JF, Abbot P, Chapman R, Dahl PH, et al. Shallow Water '06. Oceanography 2007;20(4):156–167.

[18] Shroyer EL, Moum JN, Nash JD. Nonlinear internal waves over New Jersey's continental shelf. J Geophys Res 2010;116. Doi:10.1029/2010JC006332.

[19] Ródenas JA, Garello R. Internal wave detection and location in SAR images using wavelet transform. IEEE Trans Geosci Remote Sensing 1998;36(5):1494–1507.

[20] Shroyer EL, Moum JN, Nash JD. Observations of polarity reversal in shoaling nonlinear internal waves. J Phys Oceanogr 2009;39:691–701.

[21] Ostrovsky LA, Stepanyants YA. Do internal solitons exist in the ocean? Rev Geophys 1989;27(3):293–310.

[22] Lamb KG. Shoaling solitary internal waves: on a criterion for the formation of waves with trapped cores. J Fluid Mech 2006;478:81–100.

[23] Yang YJ, Lien RC, Chang MH, Tang TY. Pressure perturbations induced by large-amplitude solitary internal waves. J Phys Oceanogr 2011;In prep.

[24] Holloway PE, Pelinovsky E, Talipova T. A generalized Korteweg-de Vries model of internal tide transformation in the coastal zone. J Geophys Res 1999;104(C8):18333–18350.

[25] Grimshaw R, Pelinovsky E, Talipova T. Modelling internal solitary waves in the coastal ocean. Surv Geophys 2007;28:273–298. Doi:10.1007/s10712-007-9020-0.